Automatic numerical focus plane estimation in digital holographic microscopy using calibration beads

Dylan Brault, Corinne Fournier, Thomas Olivier, Nicolas Faure, Sophie Dixneuf, Louis Thibon, Loic Mees, Loïc Denis

Automatic numerical focus plane estimation in digital holographic microscopy using calibration beads

DYLAN BRAULT[1], CORINNE FOURNIER[1,*], THOMAS OLIVIER[1], NICOLAS FAURE[2], SOPHIE DIXNEUF[3], LOUIS THIBON[1], LOÏC MEES[4] AND LOÏC DENIS[1]

[1] *Univ. Lyon, Hubert Curien Laboratory, UMR CNRS 5516, France.*
[2] *Centre Christophe Merieux, Grenoble, France.*
[3] *BIOASTER, Bioassays, Microsystems & Optical Engineering Unit, Lyon, France.*
[4] *Univ. Lyon, CNRS, LMFA, UMR CNRS 5509, France.*
[*] *corinne.fournier@univ-st-etienne.fr*

Abstract: We present a new method to achieve autofocus in digital holographic microscopy. The method is based on inserting calibrated objects into a sample placed on a slide. Reconstructing a hologram using the Inverse Problems Approach makes it possible to precisely locate and measure the inserted objects and thereby derive the slide plane location. Numerical focusing can then be performed in a plane at any chosen distance from the slide plane of the sample in a reproducible manner and independently of the diversity of the objects in the sample.

1. Introduction

Microscopy is routinely used in medical diagnosis in the context of infectious diseases detection and/or characterization, blood components morphological analysis and counting, or cancerous tissue analysis [1]. The need to screen large numbers of samples and/or wide areas of a sample requires automation of the analysis at each stage of the diagnosis (sample preparation, imaging, image processing, analysis and classification). However, the appearance of the sample may vary considerably depending on the nature of the sample, the imaging method, the illumination properties and the sample preparation (including fixation and staining).

Autofocusing is one of the first requirements for automation of the process. Efficient autofocusing methods may be required in particular for long-time acquisitions [2], exhaustive imaging of samples [3], or simply for the automation of microscopy systems for high throughput inspection of slides. Another reason for precise focusing in the context of automation is simply the need for the repeatability and standardization of the imaging conditions, which is crucial for automated image processing, analysis and classification.

However, autofocusing can be tricky for several reasons. When high-magnification and high-numerical aperture objectives are used (which is the case when examining blood samples, for example), the depth of field of the microscope may be less than 1 μm. In the case of brightfield microscopy of stained samples, the density, opacity, size, axial locations of the objects of interest

inside the sample may not be the same, with variations in size or in axial locations that may be greater than the depth of field. In these conditions, even the definition of the best focus becomes problematic. In some real-time focusing strategies, it may be better to measure the position of the slide surface as a reference plane to be tracked. This can be done by including additional optical elements solely dedicated to the autofocusing problem (triangulation with oblique illumination, confocal pinhole detection, dual-LED illumination, tilted sensor, etc.) [3]. These technical solutions are beyond the scope of this paper. Here we focus on techniques that require no dedicated optical elements other than the imaging system itself.

In image-based autofocusing, the best focus is typically defined by choosing a global or local criterion (combining image properties) to be maximized or minimized [3]. The efficiency of different criteria vary depending on, among others, whether the objects of interest are opaque or transparent, isolated, or embedded in a dense medium. The efficiency of the criteria may also depend on the microscopy technique or even on the illumination properties, as the image properties may vary considerably from one technique to the other.

With coherent imaging methods, like digital holography, it is possible to measure or estimate the complex amplitude of the wave diffracted by a given sample. The in-line (or Gabor) configuration [4] is the simplest to set up as, unlike the off-axis configuration, it does not require a reference beam, and can be used without any objective (lensless microscopy). It can also be adapted for use on a traditional microscope. The only requirements are a temporally and spatially coherent (or partially coherent) source and to record an out-of-focus image of the object on the sensor. Physical focusing on the sample is then no longer required, making it possible to design imaging systems without the need for an expensive automated axial positioning system with sub-micrometer resolution. However, as the hologram is the intensity image of the wave diffracted by the sample, the phase of the wave is not directly accessible and in-line digital holography requires numerical reconstructions that consist in a phase retrieval problem. This problem can be numerically solved by using alternating projection strategies or Inverse Problem Approaches (IPA) [5–7]. Even if the reconstruction of the wave is possible anywhere in the object space in in-line holographic microscopy, it is important to find a criterion that can locate a refocusing plane in a reproducible and physical meaningful way, irrespective of the method used for the reconstruction. With traditional focusing criteria [8–14], this location is likely to vary depending on the density, spatial distribution, size, and transmission of the objects.

In this paper, we present a new approach to estimate the axial distance between the focal plane of the optical system and a physical reference plane corresponding to the surface between the sample and the slide (or the coverslip, depending on the sample configuration).

This approach is based on the insertion of stable calibrated objects (spherical beads) in the sample. These beads can be reconstructed by standard object positioning algorithms that use focusing criteria [10, 11, 13]. Parametric IPA have already proven their ability to detect simple shaped objects and to accurately estimate their position and size [15–17]. The slide surface can be thus reconstructed accurately from the estimation of the position and the size of the beads. Then, the focusing reconstruction planes can be chosen relatively to this reference plane.The main advantage of this method is that it requires only one recorded hologram and provides objective information on the location of the sample. Unlike image-based criterion, it does not suffer from the influence of the type or diversity of the sample. Moreover, the positioning and sizing of several beads in the same field of view enables estimation of potential tilting of the slide surface, as well as a more precise axial location.

It is important to notice that this methodology is not adapted nor required for any microscopy situations. For dense samples (*e.g.* biological tissues), whole slide imaging, or especially with low magnification objective, the requirements for sub-micrometric focusing is not an issue, as the depth of field is more important, as well as the thickness of the sample. The main requirement would be then to find a way to keep a stable focus throughout the slide. For this, many methods mentioned previously would do the job. Moreover, in some samples, it can be difficult or undesirable to insert objects, because of the sample nature or to avoid contamination. However, our methodology is adapted to the context of automated microscopy analyses of liquid samples (*e.g.*, blood, urine, cerebrospinal fluid). As they represent an important part of the medical microscopy analyses, their automation is of major importance. In this context, our methodology, in its principle, aims at being repeatable and robust to a large diversity of size, absorption or density of the objects present in the sample, contrary to image-based methods. In the context of automation, it aims at locating, for each slide/Field Of View, a spatial reference position with a sub-micrometric resolution.

In the following section, we detail this methodology starting with the choice of the calibrated objects and ending with the reconstruction of the slide surface using an Inverse Problems Approach (IPA). Then in the third section, we present the results of simulated and experimental data on samples containing a mixture of calibration beads and biological objects.

2. Proposed methodology for reproducible axial localization of samples using in-line digital holography

Before detailing the setup and the criteria for choosing wisely the calibrated objects, we illustrate, using simulations, the need for a spatially well-defined reference plane.

2.1. Interest of a reference plane localization

In order to emphasize the need for a reference plane, 5 simulations of spherical objects holograms were computed (see Fig.1.a) using Mie modelling [18]. The illumination is a monochromatic plane wave of wavelength $\lambda = 532nm$. The 5 beads are considered in contact with the microscope slide located at $12\mu m$ from the conjugate of the camera plane (see Fig.2). The sensor plane is composed of 1024×1024 pixels with an equivalent pitch of $p = 45nm$ corresponding to a camera pixel pitch of $4.5\mu m$ and a magnification factor of 100. The 5 beads differ in radius, refractive index, and transmittance in order to mimic the diversity of biological objects. These parameters are given in Table 1. Figures 1.b display the modulus of the back propagated wave (using angular spectrum propagation [19]) in the beads cross section XZ. The slide plane is displayed by a green line which is the same for all simulations. The beads edges are represented by black dotted circles and the planes that goes through the beads center by black dotted lines. The orange and blue dashed lines represent respectively the focusing position obtained using two image-based methods GRA and ToG detailed in Sec.3.1.3. Figures 1.c show the GRA (orange dashed curves) and ToG (blue dashed curves) focusing criteria for the five holograms. As in Figures 1.b, the slide plane position (green line), the bead center plane (dotted black line) and GRA/ToG focusing positions (orange and blue dashed lines) are also displayed. These simulations show that the focusing planes positions, estimated from image-based criteria, vary according to the criterion used (GRA or ToG), according to the optical characteristics of the objects imaged (transmittance, refractive index) and according to their sizes. Even if the ToG criterion gives positions close to the center of the objects, it deviates from them differently depending on the type and size of the

	(1)	(2)	(3)	(4)	(5)
radius r (μm)	1	0.4	0.5	0.5	0.5
z (μm)	11	11.6	11.5	11.5	11.5
refractive index n	1.4	1.35	1.44	1.44	1.35
transmittance	1	0.5	1	0.01	1

Table 1. Simulations parameters for the 5 holograms of Figure 1. The transmittance parameter is defined as $t = e^{-2\pi n_i \frac{2r}{\lambda}}$ where n_i is the extinction coefficient.

objects imaged. For example, the deviation between focusing and bead center position are not negligible : up to $0.4\mu m$ for ToG and $0.5\mu m$ for GRA. In addition, the focusing functions can have several close extrema (for example, bead 2 and 4) which can lead to bias and instability in the measurement.

To detect and classify objects on a large number of varied samples, it is important to have a numerical reconstruction in a plane positioned relatively to a physical plane, for example the slide surface. This will make the technique reproducible (the same object will always give the same pattern in the reconstructed plane) and simplify the subsequent classification task. The approach we propose makes it possible to precisely estimate the upper plane of the microscope slide (or coverslip) called hereafter *the reference plane*.

2.2. Setup and choice of calibrated objects

In-line digital holographic microscopy works directly with out-of-focus images. Indeed, the refocusing step is performed numerically during the image reconstruction process. Nonetheless, the need for an accurate, reproducible, and objective focusing criteria is still crucial, even more so in the context of automation or quantitative microscopy of highly dispersed samples.

Our approach consists in inserting well-chosen calibrated objects (calibrated spherical objects) inside the sample in order to estimate their individual locations after the hologram is captured (using a precise parametric IPA). Assuming that the beads are in contact with the slide, the 3D coordinates of the bead-slide contact point can be deduced from the size and 3D location of the beads. A slide plane can then be adjusted on the set of the 3D point cloud. This reference plane is an objective, physical position, independent of specific maximum focusing criteria. Any focusing distance can be then defined relative to this reference plane.

Fig. 2 shows the proposed setup: an in-line digital holographic microscopy setup, *i.e.* a traditional microscopy setup with coherent illumination and a slight defocus. This defocus represents the distance between the actual plane of the sample and the conjugate plane of the sensor through the optical system, hereafter referred to as the *hologram plane*. In these conditions, the image recorded by the sensor is the intensity of the wave diffracted by the sample.

The choice of the calibrated object is important as it depends on the type of sample and its preparation. Spherical geometry, simplifies the detection of the object in the hologram because accurate models, as Lorenz-Mie based models are well known. Spherical calibration beads of various types are also commercially available. The diameter should be in the same range of sizes

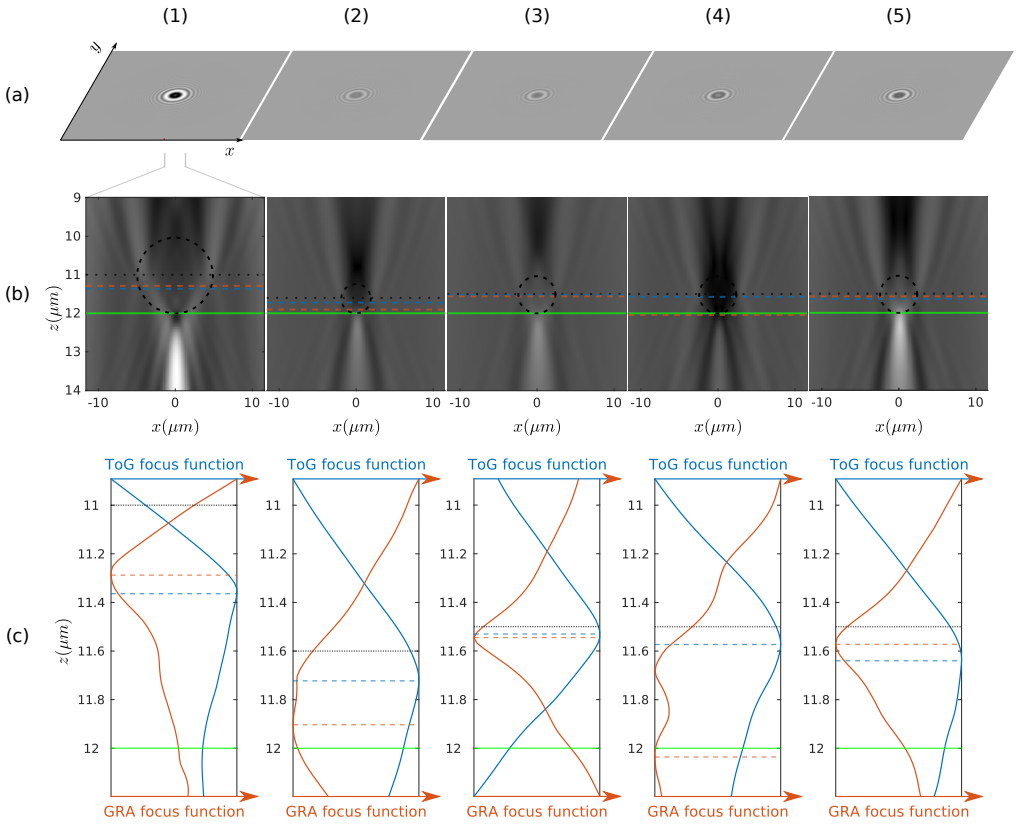

Fig. 1. Illustration of the need for an object independent reference plane : (a) in-line holograms simulated with experimental parameters given in Table 1, (b) amplitude of the back propagation of the holograms, the green line represents the slide plane, the black line and the black circles represent the beads center planes and the beads edges, the orange and blue lines represent the focus plane estimated using GRA and ToG focusing criteria, (c) evolution of the focusing function GRA (orange color) and ToG (blue color) along the direction z, the slide plane (green color) and the beads center planes (black color) are also displayed as in (b)

than the objects of interest, in order to maintain a good signal-to-noise ratio of the diffraction patterns in the hologram without leading to diffraction patterns that are too contrasted, which could affect the quality of sample reconstruction. The refractive index of the material should differ from that of the biological sample to guarantee proper discrimination of the calibration objects in the detection step.

2.3. Parametric Inverse Problems Approach to accurately locate the calibration objects

Inverse problems are a general class of problems where unknowns are linked to measurements through a known image formation model (simulating the measurements is referred to as the "direct problem"). The main idea relies on minimizing the discrepancy between the measured data and a model. If the model depends on only a few parameters and has an analytical form, the parameter can be reconstructed using parametric IPA methods [20].

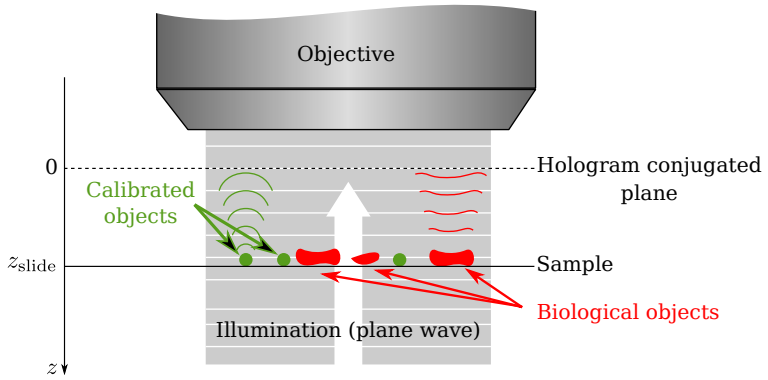

Fig. 2. Example of an in-line digital holographic upright microscope with calibrated objects inserted in the biological sample.

The reconstruction of beads from an in-line hologram amounts to estimating their spatial position (x, y, z), shape (radius r) and optical parameters (refractive index n). The diffraction pattern $\underline{\mathbf{m}}^{(i)}$ of the i^{th} spherical bead is accurately modeled by the Lorenz-Mie model [18] which depends on the set of bead parameters $\mathbf{p^{(i)}} = \{x^{(i)}, y^{(i)}, z^{(i)}, r^{(i)}, n^{(i)}\}$. This is a non-linear parametric model. It has been successfully used to reconstruct spherical object from holograms by fitting methods [15, 17] or, in a more general framework, by parametric IPA [16, 21, 22]. To guarantee completeness, a brief summary of the approach is given below.

A hologram $\mathbf{d}$ is modeled by the interference between the diffraction patterns $\{\underline{\mathbf{m}}^{(i)}\}_{i=1..N_{\text{beads}}}$ of the objects and the incident beam:

$$\mathbf{d} = \left| 1 + \sum_{\mathbf{i=1}}^{N_{\text{beads}}} \underline{\mathbf{m}}^{(i)} \right|^2 + \epsilon \tag{1}$$

where, after a proper hologram normalization step, the reference beam is assumed to be of unit magnitude, ϵ is a noise term and N_{beads} represents the number of objects in the hologram.

Accurate estimates can be obtained by maximizing a likelihood function. Assuming the noise is Gaussian, the maximum likelihood estimation of model parameters $\mathbf{p^{(i)}}$ of the i^{th} bead corresponds to weighted least squares fitting [15, 21], *i.e.* to find the parameters of a single diffraction pattern model $\underline{\mathbf{m}}^{(i)} = \underline{\mathbf{m}}\left(\mathbf{p^{(i)}}\right)$ that minimize the weighted square distance to the residuals:

$$C^2_{\mathbf{W}}(\mathbf{p^{(i)}}) = \left\| \mathbf{d} - \left| \mathbf{1} + \underline{\mathbf{m}}\left(\mathbf{p^{(i)}}\right) + \sum_{\substack{\mathbf{j=1} \\ \mathbf{j \neq i}}}^{\mathbf{N_{beads}}} \underline{\mathbf{m}}\left(\mathbf{p^{(j)}}\right) \right|^{\mathbf{2}} \right\|^{\mathbf{2}}_{\mathbf{2,W}} \tag{2}$$

where $\mathbf{W}$, the inverse of the covariance matrix of noise, allows to take into account the statistics of the noise [16]. In the case of stationary white Gaussian noise, $\mathbf{W}$ is the inverse of the noise

variance σ_ϵ^2 an $\|\boldsymbol{u}\|_{2,\mathbf{W}}^2 = (1/\sigma_\epsilon^2)\sum_{k,l} u_{k,l}^2$. To guarantee the rapid and accurate reconstruction of a set of objects, an iterative detection/localization scheme was proposed in [16]. A slightly modified version is given below.

The first step consists in coarse detection of the calibration beads inside the sample. This provides a rough estimate of all bead parameters that are then used as coordinates of the initialization points for minimization of the cost function (2) in the estimation step. Since the beads are calibrated, a narrow parameter research domain $\mathscr{D}$ can be chosen depending on the size and refractive index of the calibrated beads used experimentally. This guarantees the selection of the calibration beads among the other objects. Detection is performed by minimization of (2) in a discrete parameter space. To prevent excessive computation time due to the dimension of the parameter space, $\mathscr{D}$ must be carefully sampled. Cramér-Rao Lower Bounds make it possible to find the correct sampling step [23]. Estimating the cost function value for every subset (x, y, z, r, n) of $\mathscr{D}$ is time consuming. As the model is shift-invariant in the x and y directions, minimizing $C_{\mathbf{W}}^2$ on a (x, y) pixel grid is equivalent to maximizing the discrete cross-correlation between the data and the image formation model. Detection is then accomplished by computing a cross-correlation map for each subset (z, r, n) of $\mathscr{D}$, resulting in 5D correlation maps. In order to reduce computational complexity, the cross-correlations are computed using Fast Fourier Transforms (FFT). All the cross-correlations are saved as a z-buffer to only keep the maximum of the correlation maps on $\mathscr{D}$ in the memory. A threshold based on a percentage of the maximum value of this z-buffer is applied to limit detection to the best correlation between models and data.

After this first detection step, all the parameters are roughly estimated: (x, y) with accuracy corresponding to the pixel size, and the other parameters (z, r, n) with accuracy that depends on the sampling steps of $\mathscr{D}$.

The second step aims to refine these parameters using an optimization algorithm. The minimization of the cost function $C_{\mathbf{W}}^2$ is then performed sequentially for all the beads. At each iteration of this refinement step, the i-th bead parameters are estimated. During this step, the parameters of the beads already processed $j < i$ are set to their estimated values and the parameters of the beads that remain to be processed $j > i$ are set to the rough values obtained for them in the detection step. Consequently, the interferences between the diffraction patterns of all the beads are all accounted for in the optimization problem.

These iterative parameter estimations are more accurate than the estimation obtained during the first detection step since they are computed in the continuous parameter domain $\mathscr{D}$. In this estimation step, looser constraints than the restriction to the narrow domain $\mathscr{D}$ around the expected parameters are used in order to prevent biasing the positioning by limiting the parameters z and r to too small ranges. The optimization algorithm we used to minimize (2) in the estimation step is the SQP algorithm [24].

3. Results and Discussion

In this section, we first apply the proposed method to simulated holograms to demonstrate the robustness of our approach to samples made of objects that vary in size, transmittance and refractive index. We then apply it to experimental holograms of beads inserted in a sample of red blood cells. We compare results with state-of-the-art numerical autofocus algorithms in both simulated and experimental cases.

3.1. *Validation on simulated holograms*

3.1.1. Simulated holograms

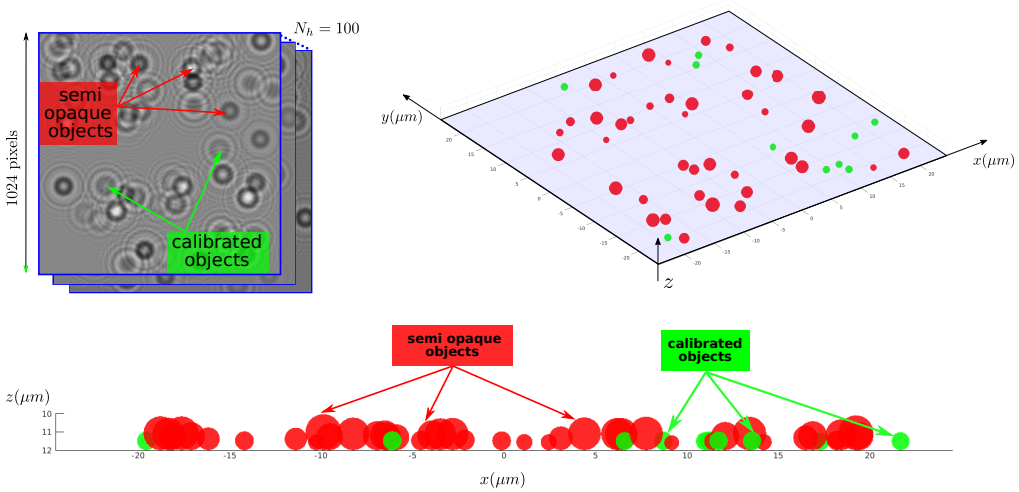

Fig. 3. Illustration of the simulation of holograms stack.

A stack of one hundred in-line holograms is simulated. For each hologram, 10 silica beads and 50 spherical objects that stand for the biological material, are simulated on a plane surface corresponding to a virtual slide perpendicular to the optical axis (see Fig 3). Lorenz–Mie models are used to generate the complex amplitude $\{\underline{\mathbf{m}}^{(i)}\}_{i=1..N_{\text{beads}}}$ of the diffracted waves on the sensor. The squared modulus of the summation of the Mie models is computed to simulate hologram intensity using eq(1).

In this simulation, the sensor plane is composed of 1024×1024 pixels with an equivalent pitch of $p = 45nm$ corresponding to a camera pixel pitch of $4.5\mu m$ and a $100\times$ magnification factor. It is located at $z_s = 12\mu m$ from the slide plane. The illumination is a monochromatic plane wave of wavelength $\lambda = 532nm$. Finally, a white Gaussian noise ϵ is added, leading to holograms with a signal-to-noise ratio of 10. All the object transversal coordinates $\{x^{(i)}, y^{(i)}\}_{i=1..N_{\text{beads}}}$ are randomly sampled on the sensor support. Objects overlap is avoided.

The objects are considered to be immersed in oil with a refractive index of 1.519. The beads parameters are those of standard silica calibration beads used for microscopy. Their mean radius is $r_b = 500nm$ and their mean refractive index is $n_b = 1.44$. To test our approach in a polydispersed case, the bead radii and refractive indices are drawn from a uniform law with a width equal to $\Delta r_b = 50nm$ for the radius and $\Delta n_b = 0.02$ for the refractive index. Their transmittance is assumed to be equal to 1 (pure phase object). The other spheres, standing for the biological sample, have more dispersed parameters also drawn from uniform distributions. The central value of the radius distribution is $r_s = 700nm$ and its width is $\Delta r_s = 600nm$. The central value of the dispersion of the refractive indices is $n_s = 1.5545$ and its width is $\Delta n_s = 0.0710$. This leads to radii in the range $[400, 1000]$ nm and refractive indices in the range $[1.519, 1.590]$. The transmittance of the spheres also varies from 0 (opaque objects) to 1 (phase object) with a uniform distribution. To better underline the diversity of the simulated samples, a summary of the parameters of these objects is given in the Table2. It should be noted that, for these simulations, the setup parameters (wavelength, pixel size, z_s) were chosen in accordance with

	silica beads (10)	other objects (50)
radius mean (nm)	500	700
range of the radii (nm)	$[475, 525]$	$[400, 1000]$
refractive index mean	1.44	1.5545
range of the refractive indices	$[1.43, 1.45]$	$[1.519, 1.590]$
transmittance mean	1	0.5
range of the transmittance	-	$[0, 1]$

Table 2. Simulation parameters for the stack of 100 holograms (illustrated in Figure 3). The bead radii and refractive indices are drawn from uniform laws. The transmittance is equal to 1 for the beads and is drawn from a uniform law for the other objects. The mean values and the ranges of the uniform laws are given in the table.

the experimental parameters in the following section.

3.1.2. Reconstruction of the reference plane

The beads are detected and their parameters estimated for each hologram using the parametric IPA described in section 2.3. Note that the other spheres representing the biological sample are not reconstructed here: in this calibration step where the focus distance is estimated, their diffraction patterns are only considered as a source of disturbance for the reconstruction of the beads. From the estimation of the couple $(z^{(i)}, r^{(i)})$ of the i^{th} bead, the z coordinate of the contact point $P^{(i)}$ of the bead-slide can be easily derived:

$$z_P^{(i)} = z^{(i)} + r^{(i)} \tag{3}$$

To be less sensitive to possible outliers in the estimations of z contact-points, the q^{th} slide z-position is estimated from the median z values:

$$z_{\text{slide}}^{(q)} = \text{median}\left(\{z_P^{(i)}\}_{i \in \text{detected beads}}\right) \tag{4}$$

3.1.3. Statistical results

Considering 100 holograms and 10 beads per hologram, 1000 beads can be detected among 5000 objects.

The detection step uses a search parameter space $\mathscr{D}$ that is centered on the average values of the ground truth parameters but that is three times bigger than the width of its distribution. This step detects the objects corresponding to the beads using a restrictive threshold coefficient on the correlation map equal to 75% of the maximum of the map, chosen in order to limit false detections. The estimation step uses much larger ranges (10 times the range of parameter distributions) so as to be less constrained.

Out of the total set of beads, 72.1 % were detected (on average 7.2 per hologram). Only 3 false detections were observed (objects that were not beads but were detected as beads) corresponding

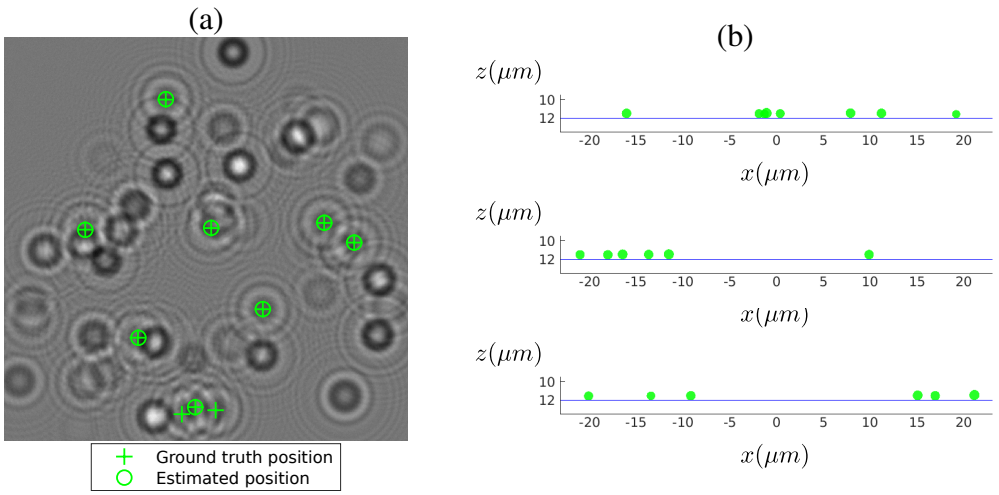

Fig. 4. (a) Example of a simulated hologram with green circles on estimated positions and crosses on ground truth positions, (b) Examples of XZ-views of the reconstructed beads

to 99.6% of true positive detections. The z contact point coordinate is computed for all the detected beads. For each hologram, the axial location of the reference plane, z_{slide}, is calculated using equation (4). An illustration is given on Figure 4.

The number of true detections could be improved by using robust detection and estimation techniques [25].

The z_{slide} is computed for each hologram and compared to the focusing distance z_{focus} estimated by two state-of-the-art algorithms, GRA and ToG, currently used in the literature:

- GRA [10] is a classical criterion for autofocusing. It is based on the search for an extremum in the integral of the magnitude of the gradient of the back-propagated field.
- ToG [13] is a sparsity criterion applied to the magnitude of the gradient of the complex back-propagated field by searching for a maximum value in the Tamura of the gradient.

For both methods, back-propagated fields are computed using angular spectrum propagation [19]. Whatever the criterion, GRA or ToG, it is based on the search for an extremum of a focus function in the stack of back propagated field maps. 50 maps were computed in the z range $[9.5, 13.5]\mu m$. A parabolic interpolation is performed on the focus function to precisely locate the extremum.

The image-based methods estimate a focus distance z_{focus} using the whole field of view, thus considering all the objects (with their diversity). Results obtained with IPA, GRA and ToG methods are displayed on the box-and-whisker plot in Figure 5. As expected, the median values of z_{slide} and z_{focus} (red line on the box and whisker) differ from one method to another : $12.00\mu m$ for IPA, $11.56\mu m$ for GRA and $11.30\mu m$ for ToG . Actually, only the IPA method produces an estimate of z_{slide}. z_{slide} is estimated with a very small bias of $2nm$, which can be considered as non-significant given the standard error. Image-based methods estimate a focus distance z_{focus}

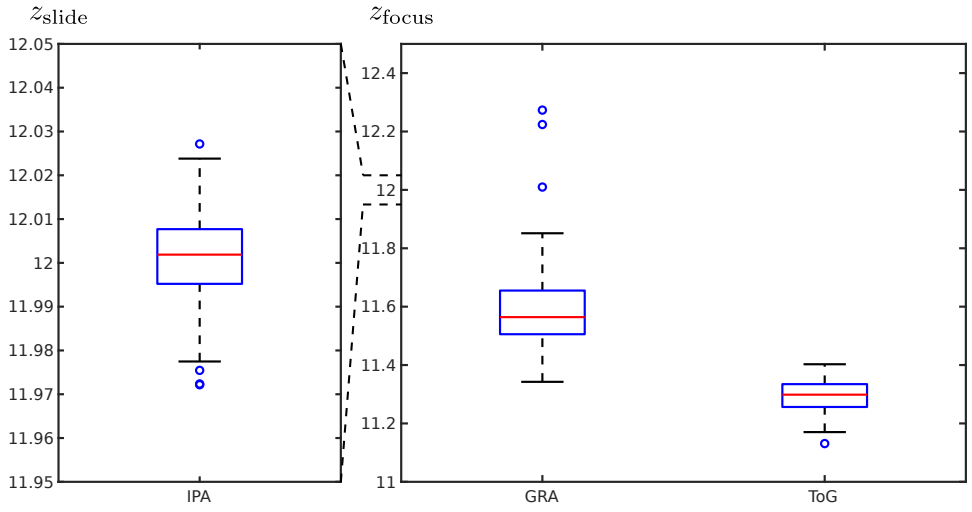

Fig. 5. Box and whiskers plot of the axial locations (in μm) of z_{slide} for IPA and of z_{focus} for GRA and ToG criteria. The red lines represent the median values, the boxes extends from the 25th to the 75th percentile, the black lines represent the non-outlier minimum and the non-outlier maximum and the circles represent the outliers. Four outliers obtained with GRA method are not represented for visualization sake.

located within the objects and thus smaller than z_{slide}. The interquartile ranges (distance between the upper and lower quartiles) are respectively $13nm$, $149nm$ and $79nm$ for IPA, GRA and ToG methods. It shows that the IPA is more accurate than image-based approaches, which makes sense because of the diversity of the simulated objects in the field of view and the global estimation of the image-based methods.

3.2. Application to experimental holograms

3.2.1. Experiment

In this section, we apply our approach to blood smear samples. The calibrated objects are mono-dispersed silica spherical microparticles with a mean diameter of 1μm . The choice of these objects was made in the context of blood smear sample observations with high magnification oil-immersion objectives. For our application, this choice has several advantages:

- The **size** (1μm) is similar to the biological objects in the sample (blood cells, platelets, bacteria, etc.) and is small enough to allow an accurate axial positioning.
- The **material** (silicon dioxyde) is dense, which allows sedimentation on the slide, non-porous (which prevents the beads from being stained), solvent and heat resistant (which prevents the beads from being damaged by the fixation process).
- The **refractive index** (1.40-1.46) is not so different from the surrounding immersion medium (1.52), which provides moderately contrasted holograms to prevent too much disturbance caused by the calibrated objects. The refractive index is also lower than the

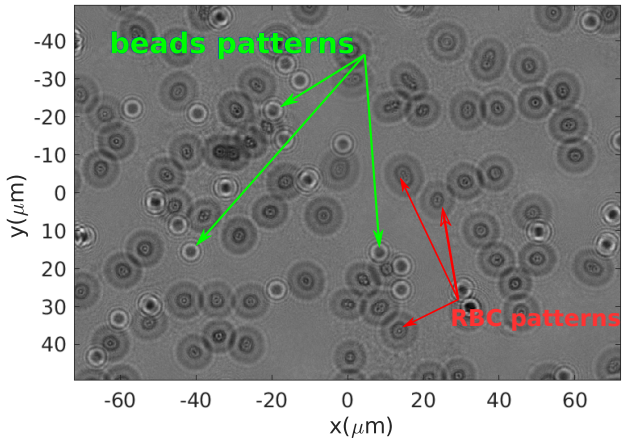

Fig. 6. Example of an experimental hologram

immersion medium refractive index, contrary to the case of fixed biological objects, which is particularly discriminating.

- The **transparency** of the silica beads is an advantage as, whatever the wavelength used, they can be considered as purely phase objects. Moreover, it is best to use transparent calibration objects to observe stained samples, as they can be more easily differentiated from the stained biological structures.

Preparation of the blood smear begins with the mixing of a small volume of blood with an appropriate dilution of silica beads in aqueous suspension. The dilutions are calibrated beforehand to obtain a representative number of beads in each field of view. A drop of this mix is then spread on a glass slide using the traditional "wedge or push" technique. The sample is then fixed with ethanol and Gram stained.

The data presented here have been acquired by scanning a single sample slide. It was imaged on a home-made microscopy system optimized for in-line digital holographic microscopy. The light source is a green LED with a narrow band (10nm) filter centered at 532nm. The illumination of the sample is done with a Köhler illumination optimized for a high spatial coherence, *i.e.* with a low angular aperture (typically 20mrad of beam divergence). The microscope objective is a 100×, 1.4NA oil immersion objective (MPLAPON 100XO, Olympus). This objective is an infinity corrected objective. The microscopy setup has two different ports. One port is designed for brightfield, in-focus microscopy, with a color sensor located in the image focal plane of a first tube lens. The other port is designed for in-line holography, with a monochrome sensor located few millimeters away from the image focal plane of a second tube lens. In these conditions, when the system is in-focus on the brightfield port, the holography port is out-of-focus with an equivalent axial shift (defocus) of $9.9\mu m$.

A set of 40 distinct fields of view has been recorded on a sensor of 3208×2200 pixels. Each field correspond to a $144\mu m \times 99\mu m$ view of the sample. Because of the mechanical stability and backlash effects of the automated XYZ-stage, it was not possible to have an axial positioning

repeatability better than $\pm 1 \mu m$ (typically) during the lateral translations of the sample on the whole explored area. A physical autofocus step was then performed on each field, using a high-precision piezoelectric objective scanner (PIFOC, PI) with a bidirectional repeatability of ±5nm and a classical focusing criteria adapted for brightfield images. This autofocusing step will not be described in detail here. However, this implies that the precision of the physical position of the slide is limited by the autofocusing accuracy. We should emphasize that this autofocus step was only necessary here to evaluate the feasibility of our approach, and is no longer necessary now that the method is validated : the autofosing can be performed numerically.

In order to compare our Inverse Problem Approach (IPA) to other autofocusing algorithms (GRA and ToG, previously described in section 3.1), we have extracted 3 sets of positioning data from each hologram, with three different approaches :

- The first set is the (x, y, z) contact point cloud corresponding to the contact point ($z_P = z+r$) estimated by parametric inverse problem approach described in subsection 2.3. An example of such a reconstruction is displayed on Figure.7.
- The second set is also a (x, y, z) point cloud corresponding to the focus estimation with the GRA criterion performed on patches extracted from each hologram (each hologram was divided into 25 non-overlapping sub-images (5×5). The patches size is 640×440 pixels.
- The third set is exactly the same as the second, but with the ToG algorithm instead of the GRA criterion.

In these conditions, we generated 40 point clouds (x, y, z) with 3 different methods that will be referred as IPA, GRA and ToG in the following. With the IPA method, we reconstructed 1129 contact point locations, randomly distributed from one field to the other. The median value is 29 contact points per field (with a minimum of 18 and a maximum of 37). The computation time of the proposed reconstruction method depends on the number of beads to reconstruct. For these experiments, with an Intel Xeon CPU 2.20GHz with 65GBytes of RAM the IPA algorithm take 7 seconds per bead (for both the detection and the estimation).

For GRA and ToG sets, it must be noticed that the reconstructed axial position are the best numerical focus obtained on the patches. In these patches, most of the pixels are occupied by red blood cells. Moreover, contrary to the IPA reconstruction of the beads, the 25 patches are equally distributed over the field. The goal here was to generate comparable sets of data for the local IPA approach and the global image-based methods (GRA and ToG). With the patch approach, the image-based algorithms are able to evaluate the focus at a more local scale. The number of locations on a field are also similar: 29 for IPA, 25 for patches approaches.

3.2.2. Reconstruction of the reference plane

For each hologram and each method (IPA, GRA, ToG), a robust plane fit was performed on the point cloud (x, y, z), using iterative re-weighted least squares with a Cauchy robust function. The plane is defined by the parametric equation $z = \hat{a}.x + \hat{b}.y + \hat{c}$, where $(\hat{a}, \hat{b}, \hat{c})$ are the estimated parameters. Parameter $\hat{c}$ is then the estimated axial position in the center of the field, which represents the contact point for the IPA, and the best focus in the center patch for GRA and ToG.

For our approach (IPA), the dispersion of the estimated contact point axial locations from the fitted plane is presented in the form of a box and whiskers plot of the residuals on Fig. 8(A). As

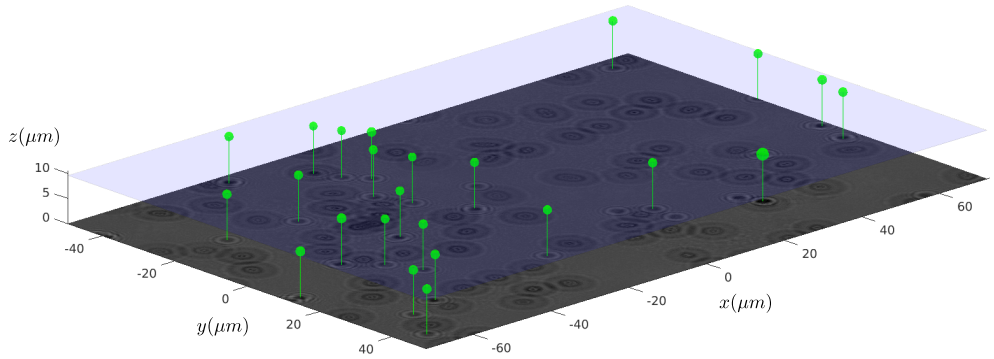

Fig. 7. Illustration of the beads reconstruction from one hologram. For visualisation purposes, the size of the beads is doubled.

can be seen, the point axial positions are close to the fitted plane but with some outliers. The plot has been cropped to exclude a few outliers with an error larger than $\pm 0.5 \mu m$ (16 outliers over 1129 beads). This behavior can be due to false detections, or faulty estimations of altered or agglomerated beads. The use of robust plane fitting is then justified, as it gives less weight to outliers. This presence of outliers can be also seen with the patch approaches (GRA, ToG), but to a lesser extent. In this case, the variability of the blood cells distribution among the patches is to be blamed, even if this distribution is quite dense and uniform. Incidentally, in the rest of our analyses, it has been chosen to use median values, rather than averages and a robust estimation of the dispersion using the median absolute deviation (MAD) of the data: $\sigma_{\text{MAD}} = 1.4826 \times \text{MAD}$.

From the IPA reconstructions, the estimated parameters of the 40 planes are presented on Fig. 8(B-D). The estimated parameters are the axial position in the center of the field ($\hat{c}$), the slope along x ($\hat{a}$) and the slope along y ($\hat{b}$). The error bars represent the estimated standard errors on these parameters, evaluated in the robust plane fitting step. Thus, these errors only depend on the accuracy of the fit, which may be related to the accuracy of the IPA reconstruction, the number of beads and their distribution within each field and the presence and number of outliers. This error must not be confused with the dispersion of the parameters measured from one field to the other (presented later).

Table 3 presents the fitted parameters evaluated on the 3 sets of data (IPA, GRA, ToG). The value and dispersion given in this table are, respectively, the median value of the parameters $(\hat{a}, \hat{b}, \hat{c})$ on the 40 holograms and the median value of the standard error on parameters found for the 40 holograms. As expected, there is a difference in the median value of the axial position between the IPA set ($9.686 \mu m$) and the GRA and ToG sets (respectively $8.973 \mu m$ and $8.635 \mu m$). Indeed, it is reasonable to find such a difference (around $1 \mu m$) as the IPA method is expected to locate the slide surface while the other methods can only locate the best focus on red blood cells whose thickness is around $2 \mu m$. What is most striking is the fact that the two image-based methods (GRA, ToG) give axial locations almost $0.34 \mu m$ apart, which is not negligible, compared with the associated errors. This means that the best-focus axial position is sensitive to the chosen image-based criterion, which is one of the problem that our autofocusing approach propose to prevent, or at least reduce. Concerning the fitting errors, it is quite low for IPA ($\pm$19nm). This tends to demonstrate that the plane fitting is quite precise, which indirectly validate our approximation about the fact that the beads are close to the slide. The higher median errors for image-based approaches ($\pm$51nm for GRA and $\pm$123nm for ToG) indicate that a precise

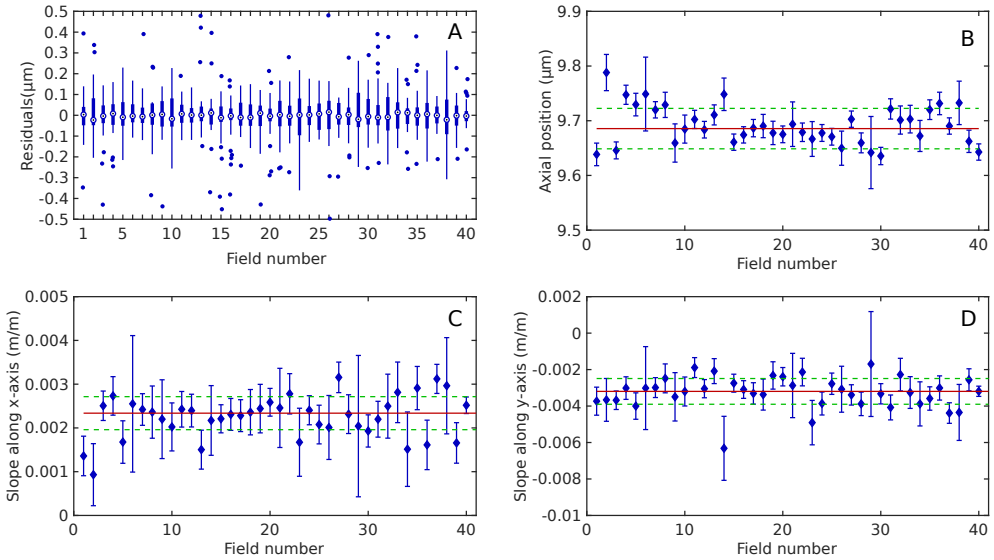

Fig. 8. Robust plane fitting results for IPA. **A:** Box and whiskers plot of the residuals of the axial locations of the reconstructed beads contact points (using eq.3) from the fitted plane as a function of the field number. The dotted circles represent the median values, the thick line extends from the 25th to the 75th percentile, the thin line extends from the non-outlier minimum from the non-outlier maximum and the circles represent the outliers. **B,C,D:** Estimated parameters on the 40 fields and the standard errors (from the robust fit). A: axial position in the middle of the field $\hat{c}$, B: slope along x direction $\hat{a}$, C: slope along y direction $\hat{b}$). The red line represents the median value over the fields, the green dashed line represents the dispersion from the median value $\pm\sigma_{\text{MAD}}$.

location using an image-based criterion on more dispersed objects (red blood cells) is a little more difficult, as the cells are thicker than the beads, more dispersed in sizes and shapes and their distribution may vary from one patch to another. Concerning the slopes of the fitted planes, the results are quite similar for the 3 sets of data. It is interesting to see that the IPA method, as well as the patches approaches with standard algorithms (GRA and ToG) are able to estimate a slope typically less than 2.5×10^{-3} (along the X-axis), which corresponds to an axial shift of only 360nm on the total width of a field ($144\mu m$).

Parameters	IPA	GRA	ToG
Axial position ($\hat{c}$) (μm)	9.686 ± 0.019	8.973 ± 0.051	8.635 ± 0.123
Slope along x ($\hat{a}$) $\times 10^{-3}$	2.337 ± 0.462	2.438 ± 0.461	2.459 ± 1.130
Slope along y ($\hat{b}$) $\times 10^{-3}$	-3.196 ± 0.683	-3.094 ± 0.671	-3.061 ± 1.641

Table 3. Fit parameters estimated from the robust plane fitting on 40 holograms with our Inverse Problem Approach (IPA) and the two state of the art algorithms (GRA, ToG) performed on 25 patches of each hologram. The estimated value are median values on the 40 holograms and the dispersion is evaluated with the median value of the standard error estimated during the robust fitting of the plane.

Finally, Table 4 presents the median value and the dispersion of the fitted parameters evaluated

with the 40 holograms. For a better illustration of the estimated tilt of the slide, the slopes have been converted into angles: θ_z being the angle between the normal of the estimated plane and the Z-axis and θ_x being the angle between the projection of this normal on the XY-plane and the X-axis. These angles can be seen as an equivalent of an azimuth (θ_x) and an elevation angle (θ_z). The median value of the axial position is the same as in table 3, but the dispersion values are obtained by calculating the σ_{MAD} of the 40 estimated parameters. These dispersion values include now the variability of the axial position of the slide and possibly of the tilt angle from one field to another. The variability of the slide position include the effect of the physical refocusing for each field. The dispersion of the axial position is still very good for IPA, with only ±37nm, which is slightly more than the ±19nm median of the standard errors previously reported on our numerical simulations, as could be expected. However, as this value includes the physical refocusing step for each field, this result indicates that the physical autofocusing step was very stable on the 40 fields under concern. For the GRA and ToG data sets, the σ_{MAD} dispersion values of the axial position over the 40 fields (±63nm for GRA, ±109nm for ToG) are similar to the median of the fitting standard errors of Table 3. Once again, ToG seems to be a little less precise in estimating the axial position. For the tilt angle θ_z, the results are very similar with a value of 0.22-0.23 degrees with the 3 methods. For the angle θ_x, the dispersion is greater, which is understandable as the projection of the normal of the plane on the XY-plane is very small and very sensitive to any error on the plane reconstruction. In particular, it must be noted that ToG is less effective in the present experimental conditions than IPA and GRA, particularly for the θ_x estimation.

As a conclusion, it must be mentioned that this study does not aim at precisely evaluating the performance of our autofocusing approach. By comparing our local IPA approach with the state-of-the-art algorithms GRA and ToG performed on image patches, it comes out that it is possible, with all 3 methods, to use a robust fit of a plane to evaluate both an axial position, as well as a very small tilt of the slide, with a pretty good repeatability on 40 non-overlapping fields-of-view of the same slide. As expected, there is a difference in the axial locations with IPA and standard approaches. Indeed, the IPA aims at locating the slide surface while the standard approaches aims at locating the best focus on dispersed objects (blood cells). While the tilt angle of the slide is quite precisely evaluated (except for ToG, which is less precise here), the error on the estimated parameters of the fit tend to indicate that the axial position of the slide is more precisely evaluated with our approach. This last point indicates also that a major hypothesis of our approach seems to be validated: except for some rare outliers that could be detected and filtered, the axial positions of the beads are close to a single plane with a good stability over the 40 analysed fields. Finally, the IPA results are not very far and quite comparable to the GRA algorithm, but it must be mentioned that the experiment was performed with a sample (blood smear) in which the most represented objects (red blood cells) were eventually very similar and quite uniformly distributed. As demonstrated on the simulations of section 3.1, the efficiency of GRA and ToG algorithms can really degrade with more dispersed biological objects.

4. Conclusion

This article presents a method for estimating the position of the plane on which the sample is placed. It is based on the insertion and detection of calibration beads in a biological sample. Estimating the location and size of the beads using a parametric IPA makes it possible to accurately reconstruct the surface of the slide on which the beads and the biological sample are placed. Knowledge of the location of this reference plane allows the user to objectively choose the position of the reconstruction plane.

Parameters	IPA	GRA	ToG
Axial position ($\hat{c}$) (μm)	9.686 ± 0.037	8.973 ± 0.063	8.635 ± 0.109
θ_z (degrees)	0.224 ± 0.035	0.227 ± 0.018	0.221 ± 0.072
θ_x (degrees)	125.6 ± 7.2	129.8 ± 10.6	130.5 ± 23.0

Table 4. Median value and dispersion on various parameters amongst the 40 fields tested. The dispersion is still evaluated with σ_{MAD}. θ_z is the angle between the Z-axis (optical axis) and the normal to the plane surface. θ_x is the angle between the X-axis direction and the projection of the normal on the horizontal plane (XY-plane).

Unlike other approaches, the reference plane is independent of the type of objects present in the biological sample and therefore enables reproducible focusing on an objective physical surface, which could be useful for whole slide imaging, drift compensation or automated high-throughput sample classification. Moreover, it also makes it possible to estimate a tilt of the slide, which could allow tilt corrections.

The study provides proof of the feasibility of the method. Its limits in terms of required density and variety of objects in the field still need to be studied. The proposed methodology was applied to an in-line holographic configuration, but it is also applicable to off-axis holography when the samples are composed of objects of different shapes and different optical characteristics. Moreover, this methodology is complementary and compatible with other calibration approaches that use spherical objects to evaluate spatially-variant aberrations in the context of wide-field microscopy [26]. Indeed, in degraded microscopy situations (low magnification and significant aberrations), the accurate location of the slide plane would require that aberrations are calibrated and modeled in the inversion method.

The need for inserting calibrated objects inside a sample or using known patterns engraved on the slides adds additional experimental complexity or cost to the sample preparation step. However, the method proposed here offers interesting perspectives for reconstructing a slide surface that is not flat.

It must be noted that this approach does not particularly requires mono-dispersed calibration beads because the size of the beads are evaluated and taken into account in the reconstruction of the slide plane. Moreover, depending on the application, the use of purely absorbing objects of micrometer or even sub-micrometer sizes is also possible.

5. Backmatter

Acknowledgement. The algorithmic tools (optimization strategies, models, regularizations) presented in this work have been implemented within the framework of the Matlab library GlobalBioIm [27, 28] (https://biomedical-imaging-group.github.io/GlobalBioIm/index.html).

Funding. This work has been funded by the Auvergne-Rhône-Alpes region, France, under project DIAGHOLO. It was also performed within the framework of the LABEX PriMES (ANR-11-LABX-0063) of Université de Lyon, within the program "Investissements d'Avenir"(ANR-11-IDEX-0007) operated by the French National Research Agency (ANR).

Disclosures. The authors declare no conflicts of interest.

References

1. N. Dey, A. Ashour, and A. Singh, "Digital analysis of microscopic images in medicine," J. Adv. Microsc. Res. **10**, 1–13 (2015).
2. P. Bon, N. Bourg, S. Lécart, S. Monneret, E. Fort, J. Wenger, and S. Lévêque-Fort, "Three-dimensional nanometre localization of nanoparticles to enhance super-resolution microscopy," Nat. Commun. **6**, 7764– (2015).
3. Z. Bian, C. Guo, S. Jiang, J. Zhu, R. Wang, P. Song, Z. Zhang, K. Hoshino, and G. Zheng, "Autofocusing technologies for whole slide imaging and automated microscopy," J. Biophotonics **13**, e202000227 (2020).
4. D. Gabor, "A New Microscopic Principle," Nature **161**, 777–778 (1948).
5. J. R. Fienup, "Phase retrieval algorithms: a comparison," Appl. Opt. **21**, 2758–2769 (1982).
6. T. Latychevskaia and H.-W. Fink, "Solution to the Twin Image Problem in Holography," Phys. Rev. Lett. **98**, 233901 (2007).
7. F. Momey, L. Denis, T. Olivier, and C. Fournier, "From fienup's phase retrieval techniques to regularized inversion for in-line holography: tutorial," J. Opt. Soc. Am. A **36**, D62–D80 (2019).
8. J. Gillespie and R. A. King, "The use of self-entropy as a focus measure in digital holography," Pattern recognition letters **9**, 19–25 (1989).
9. F. Dubois, C. Schockaert, N. Callens, and C. Yourassowsky, "Focus plane detection criteria in digital holography microscopy by amplitude analysis," Opt. Express **14**, 5895–5908 (2006).
10. P. Langehanenberg, G. von Bally, and B. Kemper, "Autofocusing in digital holographic microscopy," 3D Res. **2**, 1–11 (2011).
11. F. Lamadie, L. Bruel, and M. Himbert, "Digital holographic measurement of liquid–liquid two-phase flows," Opt. Lasers Eng. **50**, 1716–1725 (2012).
12. P. Memmolo, M. Paturzo, B. Javidi, P. A. Netti, and P. Ferraro, "Refocusing criterion via sparsity measurements in digital holography," Opt. letters **39**, 4719–4722 (2014).
13. Y. Zhang, H. Wang, Y. Wu, M. Tamamitsu, and A. Ozcan, "Edge sparsity criterion for robust holographic autofocusing," Opt. letters **42**, 3824–3827 (2017).
14. R. Malik, P. Sharma, S. Poulose, S. Ahlawat, and K. Khare, "A practical criterion for focusing of unstained cell samples using a digital holographic microscope," J. Microsc. **279**, 114–122 (2020).
15. S.-H. Lee, Y. Roichman, G.-R. Yi, S.-H. Kim, S.-M. Yang, A. Van Blaaderen, P. Van Oostrum, and D. G. Grier, "Characterizing and tracking single colloidal particles with video holographic microscopy," Opt. express **15**, 18275–18282 (2007).
16. F. Soulez, L. Denis, C. Fournier, É. Thiébaut, and C. Goepfert, "Inverse-problem approach for particle digital holography: accurate location based on local optimization," JOSA A **24**, 1164–1171 (2007).
17. F. C. Cheong, B. J. Krishnatreya, and D. G. Grier, "Strategies for three-dimensional particle tracking with holographic video microscopy," Opt. express **18**, 13563–13573 (2010).
18. F. Slimani, G. Gréhan, G. Gouesbet, and D. Allano, "Near-field lorenz-mie theory and its application to microholography," Appl. optics **23**, 4140–4148 (1984).
19. J. W. Goodman, "Introduction to fourier optics, roberts & co," Publ. Englewood, Colo. (2005).
20. A. Tarantola, *Inverse problem theory and methods for model parameter estimation* (SIAM, 2005).
21. F. Soulez, L. Denis, É. Thiébaut, C. Fournier, and C. Goepfert, "Inverse problem approach in particle digital holography: out-of-field particle detection made possible," JOSA A **24**, 3708–3716 (2007).
22. L. Méès, N. Grosjean, D. Chareyron, J.-L. Marié, M. Seifi, and C. Fournier, "Evaporating droplet hologram simulation for digital in-line holography setup with divergent beam," JOSA A **30**, 2021–2028 (2013).
23. C. Fournier, L. Denis, and T. Fournel, "On the single point resolution of on-axis digital holography," JOSA A **27**, 1856–1862 (2010).
24. J. Nocedal and S. Wright, *Numerical optimization* (Springer Science & Business Media, 2006).
25. A. J. Fitch, A. Kadyrov, W. J. Christmas, and J. Kittler, "Fast robust correlation," IEEE Transactions on Image Process. **14**, 1063–1073 (2005).
26. G. Zheng, X. Ou, R. Horstmeyer, and C. Yang, "Characterization of spatially varying aberrations for wide field-of-view microscopy," Opt. Express **21**, 15131–15143 (2013). Publisher: Optical Society of America.
27. M. Unser, E. Soubies, F. Soulez, M. McCann, and L. Donati, "Globalbioim: A unifying computational framework for solving inverse problems," in *Computational Optical Sensing and Imaging,* (Optical Society of America, 2017), pp. CTu1B–1.
28. E. Soubies, F. Soulez, M. T. McCann, T.-a. Pham, L. Donati, T. Debarre, D. Sage, and M. Unser, "Pocket guide to solve inverse problems with globalbioim," Inverse Probl. **35**, 104006 (2019).